Title	Incompressible moving boundary flows with the finite volume particle method
Author(s)	Quinlan, Nathan J.; Nestor, Ruairi M.
Publication Date	2010-03-24
Publication Information	Nestor, R. M., & Quinlan, N. J. Incompressible moving boundary flows with the finite volume particle method. Computer Methods in Applied Mechanics and Engineering, In Press, Corrected Proof.
Publisher	Elsevier
Link to publisher's version	http://dx.doi.org/10.1016/j.cma.2010.03.015
Item record	http://hdl.handle.net/10379/1091

Incompressible Moving Boundary Flows with the Finite Volume Particle Method

Ruairi M. Nestor, Nathan J. Quinlan*

Mechanical and Biomedical Engineering, College of Engineering and Informatics, National University of Ireland, Galway

Abstract

Mesh-free methods offer the potential for greatly simplified modeling of flow with moving walls and phase interfaces. The finite volume particle method (FVPM) is a mesh-free technique based on interparticle fluxes which are exactly analogous to intercell fluxes in the mesh-based finite volume method. Consequently, the method inherits many of the desirable properties of the classical finite volume method, including implicit conservation and a natural introduction of boundary conditions via appropriate flux terms. In this paper, we describe the extension of FVPM to incompressible viscous flow with moving boundaries. An arbitrary Lagrangian-Eulerian approach is used, in conjunction with the mesh-free discretisation, to facilitate a straightforward treatment of moving bodies. Non-uniform particle distribution is used to concentrate computational effort in regions of high gradients. The underlying method for viscous incompressible flow is validated for a lid-driven cavity problem at Reynolds numbers of 100 and 1000. To validate the simulation of moving boundaries, flow around a translating cylinder at Reynolds numbers of 20, 40 and 100 is modeled. Results for pressure distribution, surface forces and vortex shedding frequency are in good agreement with reference data from the literature and FVPM results for an equivalent flow around a stationary cylinder. The results demonstrate the capability of FVPM to simulate large wall motions accurately in an entirely mesh-free framework.

Key words: finite volume particle method, mesh-free method, moving boundaries, lid-driven cavity, flow over cylinder,

1. Introduction

In this article we describe a validated development of the mesh-free finite volume particle method (FVPM) for incompressible flow around moving bodies. Mesh-free methods for computational fluid dynamics (CFD) represent the fluid

---

*Corresponding author

Email address: `nathan.quinlan@nuigalway.ie` (Nathan J. Quinlan)

with a set of moving nodes or particles rather than with a fixed mesh of nodes with predefined connectivity. Mesh-free methods are particularly suited to flows with free surfaces, moving walls and multiple phases because interfaces can be treated without remeshing or special geometric treatments. Furthermore, they have the potential to reduce the cost of expert human effort required for mesh generation.

Smoothed particle hydrodynamics (SPH) is the most mature and widely applied mesh-free method for CFD. SPH, proposed independently by Gingold and Monaghan [1] and Lucy [2], is a fully Lagrangian technique in which the particles have fixed mass, and local conservation is enforced through pairwise symmetric particle interactions. Gradient approximations for the flow variables at each particle are computed on the basis of a smoothed interpolation process. SPH was originally developed for unbounded problems in astrophysics, but has seen extensions to industrially relevant applications. A recent review of SPH is given by Monaghan [3]. The method has yielded accurate predictions of challenging realistic problems including complex 3D unsteady free-surface flows [4].

Boundary conditions in SPH are typically enforced through fictitious particles on the boundary and/or outside the fluid domain. This approach is difficult to generalise to arbitrary geometries. The basic SPH gradient approximation is not exact for constant-valued functions (i.e. not zero-order consistent) [5] and numerical error does not necessarily vanish as the particle size tends to zero [6]. The consequences of this behaviour are not fully understood. All particle-based methods incur relatively high computational costs because of the use of a large computational stencil, which must be reconfigured after every particle position update. The cost is compounded by the facts that the initial particle distribution evolves with the flow, and that SPH-like methods suffer degraded convergence and/or conservation properties in the presence of non-uniform particle distributions. Consequently, it is not straightforward to employ a heterogeneous particle distribution to allocate computational effort economically to the spatial regions where it is most needed.

These problems have motivated the development of mesh-free particle schemes with improved accuracy, simpler boundary condition implementations, and a capacity for non-uniform particle distributions. These include the corrected SPH schemes of Randles and Libersky [7] and Bonet and Lok [8], which ensure first-order consistency at the expense of conservation. Other authors have developed flux-based formulations including the smooth volume integral conservation method of Ismagilov [9], the Riemann-SPH schemes of Vila [10] and Monaghan [11], and the finite volume particle method (FVPM) of Hietel *et al.* [12]. In this article we focus on the FVPM, which maintains conservation even when particle size and particle overlap are not uniform.

In FVPM, the fluid is represented by a set of particles, which are associated with normalised, overlapping, compactly supported kernel functions. The particles are viewed as discrete volumes for which the governing equations are written in integral form, weighted by test functions. Particle interactions are defined in terms of fluxes, which are weighted depending on the overlap of the

kernel supports. The FVPM is closely analagous to the classical finite volume method (FVM) and inherits many of its desirable properties, including exact conservation and a natural introduction of boundary conditions via appropriate flux terms. Furthermore, well-established developments for traditional CFD methods, such as upwind flux formulations, may be used in the FVPM without modifications. The basic FVPM scheme has been extended to incorporate adaptive variation of the particle support radius [13], moving boundaries in inviscid compressible flow [14, 15], a projection technique for incompressible flow [16, 17], and higher-order accuracy and viscous flow [18].

Many important and challenging applications of fluid dynamics are characterised by incompressible viscous flow with moving walls or interfaces. These include flow in blood vessels, medical devices and marine systems. In this article, we describe a development of the finite volume particle method with pressure projection for incompressible viscous flow with moving boundaries (section 2). The mesh-free character of the FVPM is exploited in an arbitrary Lagrangian-Eulerian (ALE) framework to handle the discretisation near the moving body. In addition, we introduce an improved formulation for the computation of particle volume, and exploit non-homogeneous particle distribution to enhance the efficiency of the method. The method is validated for moving walls by simulating flow over a cylinder translating relative to domain boundaries at Reynolds numbers from 20 to 100 (section 3). Results are compared with data for a stationary cylinder at the same Reynolds numbers.

2. The finite volume particle method

2.1. Governing equations

In the present work, we consider the application of FVPM to viscous incompressible flow. The governing continuity and momentum equations are written as

$$\nabla \cdot \mathbf{u} = 0 \tag{1}$$

and

$$\frac{\partial \mathbf{U}}{\partial t} + \nabla \cdot (\mathbf{F} - \mathbf{G}) = 0, \tag{2}$$

where $\mathbf{u} = (u \quad v)^T$ is the 2D velocity vector, $\mathbf{U} = \rho \mathbf{u}$, ρ is the density and t is time. $\mathbf{F} = (\rho \mathbf{u} \otimes \mathbf{u} + p\mathbf{I})$ represents the inviscid flux, where $\mathbf{I}$ is the $D \times D$ identity matrix, and D denotes the number of dimensions. The two-dimensional incompressible viscous flux is given by

$$\mathbf{G} = \begin{pmatrix} 2\mu \dfrac{\partial u}{\partial x} & \mu \left(\dfrac{\partial u}{\partial y} + \dfrac{\partial v}{\partial x} \right) \\ \mu \left(\dfrac{\partial u}{\partial y} + \dfrac{\partial v}{\partial x} \right) & 2\mu \dfrac{\partial v}{\partial y} \end{pmatrix}, \tag{3}$$

where μ is the dynamic viscosity.

2.2. The FVPM formulation

The FVPM was originally derived by Hietel *et al.* [12]. The formulation is outlined briefly here. In FVPM, the fluid is represented by a set of N particles. These particles are defined by compactly supported, overlapping test functions ψ_i of the form

$$\psi_i\left(\mathbf{x}, t\right) = \frac{W_i}{\sum_{j=1}^{N} W_j}, \tag{4}$$

where $W_i = W\left(\mathbf{x} - \mathbf{x}_i\left(t\right), h\right)$ is a compactly supported kernel function for particle i, centred at $\mathbf{x}_i$. The compact support radius is $2h$, where h is called the smoothing length, in keeping with the SPH convention. The denominator normalises the kernel function to ensure that the test functions form a partition of unity, i.e.

$$\sum_{i=1}^{N} \psi_i\left(\mathbf{x}, t\right) = 1. \tag{5}$$

Each particle is associated with a volume

$$V_i = \int_{\Omega} \psi_i \, d\mathbf{x}, \tag{6}$$

and a discrete value of any field variable ϕ

$$\phi_i = \frac{1}{V_i} \int_{\Omega} \phi \psi_i \, d\mathbf{x}, \tag{7}$$

which is a weighted average of ϕ over the domain Ω. ϕ_i is associated with the particle barycentre $\mathbf{b}_i$, defined as

$$\mathbf{b}_i = \frac{1}{V_i} \int_{\Omega} \mathbf{x} \psi_i \, d\mathbf{x}. \tag{8}$$

Denoting as $\mathbf{F}_{ij}$ an approximation for the Eulerian inviscid flux $\mathbf{F}$ between particles i and j, the ALE inviscid flux is $\mathbf{F}_{ij} - \bar{\mathbf{U}}_{ij}\bar{\dot{\mathbf{x}}}_{ij}$, where the $\bar{\mathbf{U}}_{ij}\bar{\dot{\mathbf{x}}}_{ij}$ term is the convection due to the particle motion. The particle velocity $\dot{\mathbf{x}}$ is not necessarily equal to the material velocity $\mathbf{u}$. Following Teleaga and Struckmeier [14], $\bar{\mathbf{U}}_{ij}$ and $\bar{\dot{\mathbf{x}}}_{ij}$ are defined as the averages $\frac{1}{2}(\mathbf{U}_i + \mathbf{U}_j)$ and $\frac{1}{2}(\dot{\mathbf{x}}_i + \dot{\mathbf{x}}_j)$ respectively. Introducing $\boldsymbol{\mathcal{F}}(\mathbf{U}_i, \mathbf{U}_j)$ to denote a numerical approximation to $\mathbf{F}_{ij} - \bar{\mathbf{U}}_{ij}\bar{\dot{\mathbf{x}}}_{ij}$, Hietel *et al.* [12] derived the semi-discrete form of the FVPM for inviscid flow as

$$\frac{d}{dt}\left(V_i \mathbf{U}_i\right) = -\sum_{j=1}^{N} \boldsymbol{\beta}_{ij}\left(\boldsymbol{\mathcal{F}}(\mathbf{U}_i, \mathbf{U}_j)\right) - \boldsymbol{\beta}_i^b \boldsymbol{\mathcal{F}}_i^b, \tag{9}$$

where

$$\boldsymbol{\beta}_{ij} = \int_{\Omega} \frac{\psi_i \nabla W_j - \psi_j \nabla W_i}{\sum_{k=1}^{N} W_k} d\mathbf{x} \tag{10}$$

are interaction vectors which weight the flux exchanged between particle i and each of its neighbours j. The interaction vector $\boldsymbol{\beta_{ij}}$ between particles i and j is

analagous to the cell interface area vector which weights intercell fluxes in the classical finite volume method [19]. Eq. (10) is typically evaluated by numerical integration. In Eq. (9), $\boldsymbol{\beta}_i^b$ is the particle-boundary interaction vector and $\boldsymbol{\mathcal{F}}_i^b$ is an approximation for the boundary flux (boundary conditions are discussed in full in section 2.7).

The appearance of the particle volume inside the time derivative in Eq. (9) means that an additional equation is required for the rate of change of the particle volume. Hietel *et al.* [12] show that this can be obtained by differentiating Eq. (6) with respect to time, yielding

$$\frac{d}{dt}V_i = \sum_{j=1}^{N}\left(\boldsymbol{\gamma}_{ij}\cdot\dot{\mathbf{x}}_j - \boldsymbol{\gamma}_{ji}\cdot\dot{\mathbf{x}}_i\right), \tag{11}$$

where $\boldsymbol{\gamma}_{ij}$ is introduced as

$$\boldsymbol{\gamma}_{ij} = \int_{\Omega}\psi_i\frac{\nabla W_j}{\sum_{k=1}^{N}W_k}d\mathbf{x}. \tag{12}$$

The defintions of γ_{ij} and β_{ij} imply that $\beta_{ij} = \gamma_{ij} - \gamma_{ji}$. Typically, the particle volumes are updated by time integration of Eq. (11) (This point is discussed further, and an alternative formulation is introduced, in section 2.3.) Additonally, in the present work, they are reinitialised at intervals of 20 timesteps by numerical integration of Eq. (6).

Hietel *et al.* [12] and Teleaga [15] have shown that the FVPM enforces global conservation, i.e.

$$\frac{d}{dt}\left(\sum_{i=1}^{N}V_i\mathbf{U}_i\right) = -\int_{\partial\Omega}\mathbf{F}\,d\eta, \tag{13}$$

where $\partial\Omega$ is the domain boundary and η is the boundary coordinate, provided that the numerical flux function $\boldsymbol{\mathcal{F}}$ and the interaction vectors satisfy certain conditions. The numerical flux function must satisfy the symmetry condition

$$\boldsymbol{\mathcal{F}}(\mathbf{U}_i,\mathbf{U}_j) = \boldsymbol{\mathcal{F}}(\mathbf{U}_j,\mathbf{U}_i), \tag{14}$$

which is typically the case for numerical flux functions developed for finite volume methods. The interaction vectors must satisfy the following two conditions:

$$\boldsymbol{\beta}_{ij} = -\boldsymbol{\beta}_{ji}, \tag{15}$$

$$\sum_{i=1}^{N}\boldsymbol{\beta}_{ij} = 0. \tag{16}$$

Condition (15) ensures that particle interactions are symmetric, and condition (16) is analogous to the requirement in the conventional FVM that the faces of a finite volume form a closed surface. Condition (16) is difficult to satisfy in practice because errors are introduced by numerical integration of Eq. (10). Violation of the conditions has been shown to result in unphysical

oscillations in shock tube results [16, 15, 20]. Correction procedures have been proposed by Keck [17] and Teleaga [15], which allow conditions (15) and (16) to be satisfied without resort to highly accurate numerical integration. The correction of Teleaga [15] is used for the results presented in this paper, and the interaction vectors $\boldsymbol{\beta}_{ij}$ are computed using a Gaussian quadrature procedure. 6^D integration points are used in each particle overlap region.

2.3. Particle volume rate of change

In the present work, the inviscid flux contribution due to particle motion is based on the average particle motion $\bar{\dot{\mathbf{x}}}_{ij}$ at each particle interface. This form of the discrete scheme has been used in previous FVPM work by Teleaga [15] and Teleaga and Struckmeier [14]. However, it is easily verified that when Eq. (11) for the particle volume rate of change is used in conjunction with the discrete FVPM defined by Eq. (9), uniform states are not preserved.

Considering a set of particles far from boundaries with uniform $\mathbf{U}$ and non-uniform particle motion so that $\dot{\mathbf{x}}_i \neq \dot{\mathbf{x}}_j$, the uniform state of $\mathbf{U}$ should be preserved regardless of the particle motion. The rate of change of $\mathbf{U}_i$ is given by the product rule

$$\frac{d\mathbf{U}_i}{dt} = \frac{1}{V_i} \left(\frac{d(V_i \mathbf{U}_i)}{dt} - \mathbf{U}_i \frac{dV_i}{dt} \right). \tag{17}$$

With Eq. (11) for dV_i/dt and Eq. (9) for $d(V_i\mathbf{U}_i)/dt$, Eq. (17) becomes

$$\frac{d\mathbf{U}_i}{dt} = \frac{1}{V_i} \left(-\sum_{j=1}^{N} \left(\boldsymbol{\beta}_{ij} \left(\mathbf{F}_{ij} - \bar{\mathbf{U}}_{ij} \bar{\dot{\mathbf{x}}}_{ij} \right) \right) - \mathbf{U}_i \sum_{j=1}^{N} \left(\boldsymbol{\gamma}_{ij} \cdot \dot{\mathbf{x}}_j - \boldsymbol{\gamma}_{ji} \cdot \dot{\mathbf{x}}_i \right) \right). \tag{18}$$

(Since $\mathbf{U}$ is uniform, the numerical flux $\boldsymbol{\mathcal{F}}$ is equal to the exact flux $\mathbf{F} - \mathbf{U}\dot{\mathbf{x}}$.) The term $\sum_{j=1}^{N} \boldsymbol{\beta}_{ij} \mathbf{F}_{ij}$ is zero due to the assumption of uniform $\mathbf{U}$ and condition (16) for the interaction vectors. Replacing $\bar{\mathbf{U}}_{ij}$ with $\mathbf{U}_i$ and $\boldsymbol{\beta}_{ij}$ with $\boldsymbol{\gamma}_{ij} - \boldsymbol{\gamma}_{ji}$, it follows that

$$\begin{aligned} \frac{d\mathbf{U}_i}{dt} &= \frac{1}{V_i} \sum_{j=1}^{N} \left((\boldsymbol{\gamma}_{ij} - \boldsymbol{\gamma}_{ji}) \frac{\mathbf{U}_i (\dot{\mathbf{x}}_i + \dot{\mathbf{x}}_j)}{2} - \mathbf{U}_i (\boldsymbol{\gamma}_{ij} \cdot \dot{\mathbf{x}}_j - \boldsymbol{\gamma}_{ji} \cdot \dot{\mathbf{x}}_i) \right) \\ &= \frac{\mathbf{U}_i}{2V_i} \sum_{j=1}^{N} \left(\boldsymbol{\gamma}_{ij} \cdot \dot{\mathbf{x}}_i + \boldsymbol{\gamma}_{ji} \cdot \dot{\mathbf{x}}_i - \boldsymbol{\gamma}_{ij} \cdot \dot{\mathbf{x}}_j - \boldsymbol{\gamma}_{ji} \cdot \dot{\mathbf{x}}_j \right) \neq 0. \end{aligned} \tag{19}$$

However, in the present work, we use the approximation

$$\frac{d}{dt} V_i = \sum_{j=1}^{N} \boldsymbol{\beta}_{ij} \cdot \bar{\dot{\mathbf{x}}}_{ij}, \tag{20}$$

where $\bar{\dot{\mathbf{x}}}_{ij}$ denotes the average of particle velocities at i and j. This approach, in conjunction with Eq. (9), preserves uniform states for $\dot{\mathbf{x}}_i \neq \dot{\mathbf{x}}_j$, as the following

analysis shows:

$$\begin{aligned}
\frac{d\mathbf{U}_i}{dt} &= \frac{1}{V_i}\left(-\sum_{j=1}^{N}\boldsymbol{\beta}_{ij}\left(\mathbf{F}_{ij}-\bar{\mathbf{U}}_{ij}\bar{\mathbf{x}}_{ij}\right)-\mathbf{U}_i\sum_{j=1}^{N}\boldsymbol{\beta}_{ij}\cdot\bar{\mathbf{x}}_{ij}\right)\\
&= \frac{\mathbf{U}_i}{2V_i}\sum_{j=1}^{N}\left(\boldsymbol{\beta}_{ij}\cdot(\dot{\mathbf{x}}_i+\dot{\mathbf{x}}_j)-\boldsymbol{\beta}_{ij}\cdot(\dot{\mathbf{x}}_i+\dot{\mathbf{x}}_j)\right)=0.
\end{aligned} \tag{21}$$

2.4. Higher order and viscous flow extensions

The semi-discrete FVPM for inviscid flow is defined by Eq. (9). First-order temporal accuracy is achieved if the transient term in Eq. (9) is discretised using, for example, an explicit Euler approach. First-order spatial accuracy is obtained if the numerical flux function $\mathcal{F}$ is computed on the basis of a zero order extrapolation of the discrete particle values to the particle interfaces. The FVPM has been extended to higher-order accuracy and viscous flow by Nestor *et al.* [18]. Higher-order accuracy is achieved via linear extrapolation of the variables to the particle interfaces, following the approach of van Leer [21], with a second-order explicit Runge-Kutta temporal discretisation. The gradients for linear reconstruction to the particle interfaces, as well as the velocity gradients for computation of viscous stress, are computed on the basis of the first order consistent SPH gradient approximation of Bonet and Lok [8]:

$$\nabla\phi\left(\mathbf{x}\right)\approx\sum_{j=1}^{N}V_j\left(\phi_j-\phi\left(\mathbf{x}\right)\right)\widetilde{\nabla}S_j(\mathbf{x}), \tag{22}$$

where $S_j(\mathbf{x})=S(\mathbf{x}-\mathbf{b}_j,q)$ denotes the SPH kernel function, with smoothing length q. The cubic spline kernel of Monaghan and Lattanzio [22] is a suitable choice for S. $\widetilde{\nabla}S_j(\mathbf{x})$ is the corrected gradient of the SPH kernel centred at $\mathbf{x}$ and evaluated at $\mathbf{b}_j$:

$$\widetilde{\nabla}S_j(\mathbf{x})=\left[\sum_{k=1}^{N}V_k\nabla S_k(\mathbf{x})\otimes(\mathbf{b}_k-\mathbf{x})\right]^{-1}\nabla S_j(\mathbf{x}). \tag{23}$$

Using this approach, the linear consistency constraint for the reconstruction in unstructured mesh FVMs established by Barth and Jespersen [23] is satisfied. In addition, Eq. (22) gives a gradient approximation at any point $\mathbf{x}$ in the domain, not only at the particle barycentres. Thus the SPH gradient approximation is suitable for evaluation of the viscous gradients, which must be determined at both the particle interfaces and at the boundaries.

For incompressible flow, following Drikakis and Rider [24], the Harten-Lax-van Leer (HLL) Riemann solver of Harten *et al.* [25] is used to approximate the

interparticle inviscid fluxes of the momentum equation:

$$\boldsymbol{\mathcal{F}} = \begin{cases} \mathbf{F}_l - \bar{\mathbf{U}}\bar{\mathbf{x}} & \text{if } \lambda_l, \lambda_r \geq 0, \\[2mm] \dfrac{\lambda_r \mathbf{F}_l - \lambda_l \mathbf{F}_r + \lambda_l \lambda_r \left(\mathbf{u}_r - \mathbf{u}_l\right)}{\lambda_r - \lambda_l} - \bar{\mathbf{U}}\bar{\mathbf{x}} & \text{if } \lambda_l \leq 0 \leq \lambda_r, \\[2mm] \mathbf{F}_r - \bar{\mathbf{U}}\bar{\mathbf{x}} & \text{if } \lambda_l, \lambda_r \leq 0, \end{cases} \qquad (24)$$

where $\lambda_l = \min\left(\mathbf{u}_l \cdot \mathbf{n}_{ij}, \mathbf{u}_r \cdot \mathbf{n}_{ij}, 0\right)$ and $\lambda_r = \max\left(\mathbf{u}_l \cdot \mathbf{n}_{ij}, \mathbf{u}_r \cdot \mathbf{n}_{ij}, 0\right)$. The left and right states, denoted by l and r subscripts respectively, are determined by the linear reconstruction process outlined above. No limiter function is employed in the linear reconstruction for the test cases presented in this article. In Eq. (24) the particle motion flux term is not computed using an upwind approximation, but is included as an average. In numerical experiments for lid-driven cavity flow, this approach was found to produce more accurate velocity and pressure fields than an upwind approximation.

2.5. Particle distribution control by an Arbitrary Lagrangian-Eulerian approach

The particle motion in FVPM may be set arbitrarily. Fully Lagrangian particle motion, (i.e. $\dot{\mathbf{x}} = \mathbf{u}$) has some advantages, but can result in poor particle distributions [18]. In Arbitrary Lagrangian-Eulerian (ALE) corrected particle motion schemes [13, 18] the Lagrangian particle motion is modified with a small additional velocity which prevents the formation of particle voids. In the implementation used in the present work, the particles move according to

$$\dot{\mathbf{x}}_i = \mathbf{u}_i + \mathbf{u}'_i. \qquad (25)$$

The correction velocity is given by

$$\mathbf{u}'_i = C \frac{\bar{r}_i}{\Delta t} \mathbf{R}_i, \qquad (26)$$

where

$$\bar{r}_i = \frac{1}{H_i} \sum_k r_{ik} \qquad (27)$$

is the average distance from particle i to its neighbour, and the index k denotes the neighbours of i. Δt is the timestep and C is a constant, which is typically set to 1/1000. H_i denotes the number of neighbours of particle i. The term $\bar{r}_i/\Delta t$ represents the velocity required for a particle to move by the average particle spacing $\bar{r}_i$ in a single timestep Δt. $\mathbf{R}_i$ is a dimensionless function of the particle spacing:

$$\mathbf{R}_i = -\sum_k \frac{1}{\left(\dfrac{r_{ik}}{\bar{r}_i}\right)^2} \mathbf{n}_{ik}, \qquad (28)$$

where r_{ik} and $\mathbf{n}_{ik}$ are the distance and unit vector, respectively, from $\mathbf{x}_i$ to $\mathbf{x}_k$.

Thus, ALE particle motion correction provides a weak repulsive effect to prevent the formation of particle clumps or voids. The magnitude of the correction velocity is small due to the small value of C in Eq. (26), and thus the motion of the particles remains close to Lagrangian. The effects of the correction are automatically accounted for through the ALE forumation of the FVPM. This particle motion scheme has been validated by Nestor *et al.* [18] for Poiseuille, lid-driven cavity and Taylor-Green flows.

2.6. FVPM for incompressible flow

A previous implementation of a pressure projection method in FVPM for incompressible flow has been presented by Keck [16] and Keck and Hietel [17], whose approach is in turn based on the work of Klein [26] and Schneider *et al.* [27]. In the present work, we present an implementation of a simple conventional projection method with an explicit temporal scheme, similar to that presented by Hirsch [28].

The pressure projection method was originally developed by Chorin [29]. As described by Hirsch [28] for a first order explicit temporal discretisation, the objective is to satisfy

$$\frac{\mathbf{u}^{n+1} - \mathbf{u}^n}{\Delta t} = -\nabla \cdot (\mathbf{u}^n \otimes \mathbf{u}^n) - \frac{1}{\rho}\nabla p^{n+1} + \frac{\mu}{\rho}\nabla^2 \mathbf{u}^n, \tag{29}$$

and

$$\nabla \cdot \mathbf{u}^{n+1} = 0. \tag{30}$$

Therefore, a solution for both the pressure and velocity at time level $n+1$ must be obtained simultaneously. The approach adopted in pressure projection methods is to advance Eq. (29) without the pressure term in a first stage, disregarding the divergence-free velocity condition (1). This yields an approximate intermediate velocity field $\mathbf{u}^*$:

$$\frac{\mathbf{u}^* - \mathbf{u}^n}{\Delta t} = -\nabla \cdot (\mathbf{u} \otimes \mathbf{u})^n + \frac{\mu}{\rho}\nabla^2 \mathbf{u}^n. \tag{31}$$

This velocity field does not satisfy the continuity equation (1), and must subsequently be corrected. Subtracting Eq. (31) from Eq. (29) yields

$$\mathbf{u}^{n+1} = \mathbf{u}^* - \frac{\Delta t}{\rho}\nabla p^{n+1}. \tag{32}$$

The new velocity field $\mathbf{u}^{n+1}$ is divergence-free if

$$\nabla^2 p^{n+1} = \frac{\rho}{\Delta t}\nabla \cdot \mathbf{u}^*. \tag{33}$$

The elliptic equation (33) can now be solved implicitly for p^{n+1}.

The discretisation of the pressure Poisson equation requires the definition of discrete Laplacian and divergence operators for the pressure and velocity respectively. For the Laplacian operator, the current approach consists of a FVPM

9

discretisation of the outer divergence operator and a central difference approximation for the pressure gradient at the interface between each neighbouring particle pair:

$$\left(\nabla^2 p\right)_i \approx \frac{1}{V_i}\left(\sum_{j=1}^{N} \boldsymbol{\beta}_{ij} \cdot (\nabla p)_{ij} + \boldsymbol{\beta}_i^b \cdot \nabla p_i^b\right). \tag{34}$$

The interparticle gradient $(\nabla p)_{ij}$ is approximated with a central difference

$$(\nabla p)_{ij} \approx \frac{p_j - p_i}{r_{ij}}\mathbf{n}_{ij}, \tag{35}$$

where p_j is the pressure at particle barycentre $\mathbf{b}_j$, r_{ij} is the distance between $\mathbf{b}_i$ and $\mathbf{b}_j$, and $\mathbf{n}_{ij} = \boldsymbol{\beta}_{ij}/|\boldsymbol{\beta}_{ij}|$ is the unit vector between i and j. The boundary pressure gradient ∇p_i^b must be specified as a boundary condition, as discussed in section 2.7 below. The central difference approximation for ∇p_{ij} in Eq. (34) is necessary to prevent the development of checkerboard solutions for the pressure, a well-known problem for incompressible CFD methods with colocated grids [30]. This could occur, for example, if an interpolation of discrete particle gradient approximations was used in computing ∇p_{ij}, e.g. $\nabla p_{ij} \approx (\nabla p_i + \nabla p_j)/2$.

For the discrete divergence operator, a FVPM gradient approximation is again used in conjunction with linear interpolation for $\mathbf{u}^*$ at the particle interfaces, i.e.

$$(\nabla \cdot \mathbf{u}^*)_i \approx \frac{1}{V_i}\sum_{j=1}^{N} \boldsymbol{\beta}_{ij} \cdot \left(\mathbf{u}_i^* + \frac{|\mathbf{x}_{ij} - \mathbf{b}_i|}{r_{ij}}\left(\mathbf{u}_j^* - \mathbf{u}_i^*\right)\right), \tag{36}$$

where $\mathbf{x}_{ij} = (\mathbf{b}_i + \mathbf{b}_j)/2$ in this work.

The necessary steps for the incompressible FVPM implementation are now summarised. An Euler explicit temporal discretisation is assumed for brevity, though a second-order explicit Runge-Kutta scheme is employed in the current work. The pressure and velocity are updated from time n to $n + 1$ by the following sequence of steps:

$$V_i^{n+1} = V_i^n + \Delta t\frac{dV_i}{dt}^n \tag{37}$$

$$\mathbf{U}_i^* = \frac{1}{V_i^{n+1}}\left(V_i^n\mathbf{U}_i^n + \Delta t\frac{d(V_i\mathbf{U}_i)^{*,n}}{dt}\right) \tag{38}$$

$$\mathbf{x}_i^{n+1} = \mathbf{x}_i^n + \Delta t\dot{\mathbf{x}}_i^n \tag{39}$$

$$\nabla^2 p_i^{n+1} = \frac{\rho}{\Delta t}\nabla \cdot \mathbf{u}_i^* \tag{40}$$

$$\mathbf{u}_i^{n+1} = \mathbf{u}_i^* - \frac{\Delta t}{\rho}\nabla p_i^{n+1} \tag{41}$$

where $d(V_i\mathbf{U}_i)^{*,n}/dt$ is computed from Eq. (9) without the pressure term in the flux function $\mathcal{F}$. In the present work, the solution to the discretised Eq. (40) is obtained with the LASPACK implementation of GMRES algorithm [31].

The timestep Δt is restricted by the CFL stability condition [28]

$$\Delta t \leq 0.3 \frac{\min(h)}{\max(\|\mathbf{u}\|)}, \tag{42}$$

and the viscous diffusion condition [32]

$$\Delta t \leq 0.25 \frac{\min(\rho)\min(h)^2}{\mu}. \tag{43}$$

2.7. Boundary conditions

A significant advantage of FVPM over other mesh-free methods such as SPH is that boundary conditions can be accounted for explicitly in the discrete equations, and in particular, fictitious particles outside the fluid domain are not necessary. The term $\boldsymbol{\beta}_i^b \boldsymbol{\mathcal{F}}_i^b$ in the discrete FVPM equation Eq. (9) represents a discrete approximation to a boundary integral arising in the FVPM derivation:

$$\boldsymbol{\beta}_i^b \boldsymbol{\mathcal{F}}_i^b = \int_{\partial\Omega_i} \mathbf{F}\psi_i \mathbf{n}_{ib}\, d\eta, \tag{44}$$

where $\mathbf{n}_{ib}$ is the unit normal vector pointing out of the domain. The terms $\boldsymbol{\beta}_i^b$ and $\boldsymbol{\mathcal{F}}_i^b$ are the boundary interaction vector and boundary flux respectively for particle i. Following Keck [16] and Keck and Hietel [17], the boundary coefficient $\boldsymbol{\beta}_i^b$ for particle i may be computed from

$$\boldsymbol{\beta}_i^b = -\sum_{j=1}^{N} \boldsymbol{\beta}_{ij}, \tag{45}$$

which follows from condition (16). Alternatively, the boundary coefficients may be determined by direct approximation of the boundary integral in Eq. (44), assuming a constant flux along the portion of the boundary interacting with particle i. This may be accomplished using numerical integration along the boundary segment $\partial\Omega_i$ covered by the support of particle i:

$$\boldsymbol{\beta}_i^b = \int_{\partial\Omega_i} \psi_i \mathbf{n}_{ib}\, d\eta, \tag{46}$$

where $\mathbf{n}_{ib}$ is the unit normal vector at the boundary pointing out of the domain and η is the coordinate along the boundary.

For the compressible form of the momentum equation Eq. (2), appropriate conditions are imposed on the inviscid flux $\boldsymbol{\mathcal{F}}_i^b$ to satisfy the desired boundary conditions. For a wall boundary, the convective flux is zero, and only the pressure term remains in the inviscid flux. Following Teleaga [15], the inviscid boundary flux for a particle i is based on a zero-order extrapolation of the particle pressure to the wall:

$$\boldsymbol{\mathcal{F}}_i^b = p_i. \tag{47}$$

11

The boundary viscous stress may be computed with the SPH gradient approximation of Eq. (23) centred at the midpoint of the boundary segment intersecting the particle support [18]. For a free-slip wall, the shear stress at the wall is set to zero. Following Teleaga [15], moving walls are represented by an additional contribution $\left|\boldsymbol{\beta}_i^b\right|\mathbf{u}^b\cdot\mathbf{n}_{ib}$ to the particle volume rate of change in Eq. (11), where $\mathbf{u}^b$ is the boundary velocity.

The boundary conditions on the pressure Poisson equation for incompressible flow are now described. Following, for example, Anderson [33], no-slip wall boundary conditions for the pressure Poisson equation Eq. (33) are enforced via the Neumann boundary condition for the pressure:

$$\nabla p_i^b = \mu\nabla^2\mathbf{u}_i^b. \tag{48}$$

For an inlet boundary condition, the situation is similar to a no-slip wall in that the velocity components are prescribed, and thus Eq. (48) is applied for the presure gradient [30]. For free-slip walls, a homogeneous Neumann boundary condition is applied for the pressure. For outlet boundary conditions, several formulations exist. In previous incompressible FVPM work [16], the outlet velocity was specified and a homogeneous Neumann boundary condition was specified for the pressure Poisson equation. However, this approach is valid only if the outlet velocity remains constant throughout the computation. Practically, this could occur for an obstacle in crossflow if the physical simulation time is small, or the domain is large in the flow-wise direction. In another approach detailed by Ferziger and Peric [30] the normal velocity gradient at the outlet is zero. This may be approximated by a zero order extrapolation from the computational nodes to the boundary. The resulting outlet mass fluxes are then adjusted so that mass conservation is satisfied globally. For the pressure Poisson equation, the pressure is specified at the outlet. We have adopted this approach in the current work.

For condition (48), the viscous term $\mu\nabla^2\mathbf{u}_i^b$ must be approximated on the boundary. This is accomplished by firstly approximating $\nabla\cdot\mathbf{u}$ at particle i and its neighbours using Eq. (22). $\nabla^2\mathbf{u}_i^b$ is then approximated on the boundary by applying Eq. (22) at $\mathbf{x}_i^b$, the midpoint of the boundary segment intersecting the support of particle i. This is a similar process to that employed in two-pass SPH viscous models [34]. A homogeneous Neumann condition ($\nabla p_i^b = 0$) simply makes a zero contribution to Eq. (34). Zero pressure at the outlet boundary may be enforced by setting the pressure gradient at nearby particles according to a simple finite difference, i.e.

$$\nabla p_i^b = -\frac{p_i}{r_{ib}}\mathbf{n}_{ib}, \tag{49}$$

where r_{ib} is the perpendicular distance from $\mathbf{b}_i$ to the boundary.

These pressure boundary conditions for the pressure Poisson are imposed via the boundary pressure gradient term in Eq. (34). Specified boundary pressure gradient values contribute to the Laplacian of pressure and are placed on the right-hand side of the discretised form of Eq. (40).
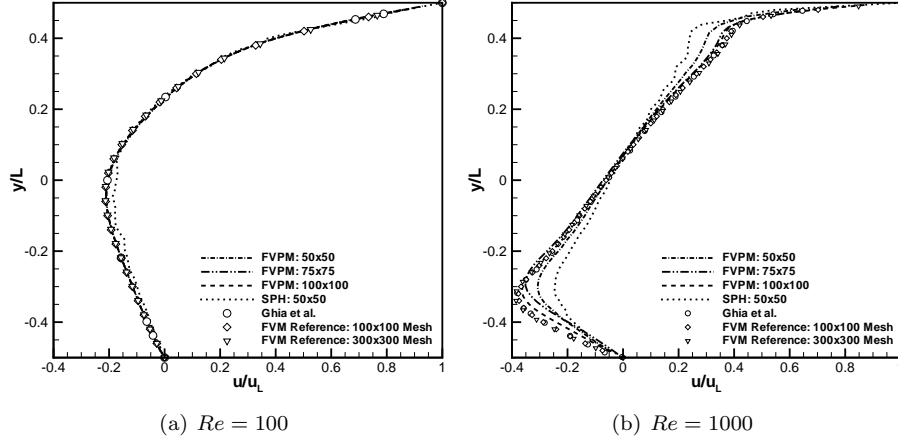
| (a) $Re = 100$ | (b) $Re = 1000$ |

Figure 1: Steady-state x-component of velocity for lid-driven cavity flow along the cavity centreline $x = 0$.

3. Numerical results

Numerical validation of the present FVPM scheme is presented in this section. Computations are presented for incompressible, viscous, laminar lid-driven cavity and circular cylinder flows. Comparisons are performed between the FVPM results and both numerical and experimental results from literature.

3.1. Lid-driven cavity

Lid-driven cavity flow at Reynolds numbers of 100 and 1000 is simulated as a validation of the present viscous incompressible FVPM implementation without moving boundaries. The problem consists of a square domain of side L with vertical and horizontal boundaries located at $x = \pm L/2$ and $y = \pm L/2$ respectively. The horizontal boundary at $y = L/2$ moves with velocity u_L tangential to the boundary. The fluid is initially at rest, but begins to circulate due to the momentum introduced by the lid motion. The flow approaches a steady state, which is characterised by a large central recirculation region. At $Re = 1000$ two additional weak recirculation regions develop in the two corners furthest from the lid.

Particle resolutions of 50×50, 75×75 and 100×100 are used to investigate the effect of particle resolution on the solution. The smoothing length of each particle is set to $h = (0.7)\Delta x$, where Δx is the initial uniform Cartesian particle spacing, and the smoothing length remains constant throughout the simulation. The particles move with corrected particle motion, Eq. (25), with the constant $C = 1/1000$ in Eq. (26). The boundary interaction vectors are determined by numerical integration of Eq. (46).
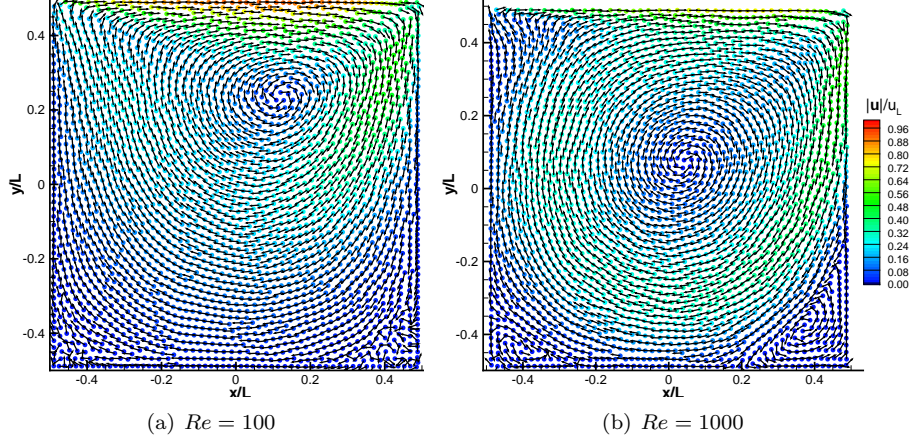
Figure 2: Velocity fields for steady state lid-driven cavity flow with 50×50 particles. For clarity, the velocity vectors are shown with uniform length.
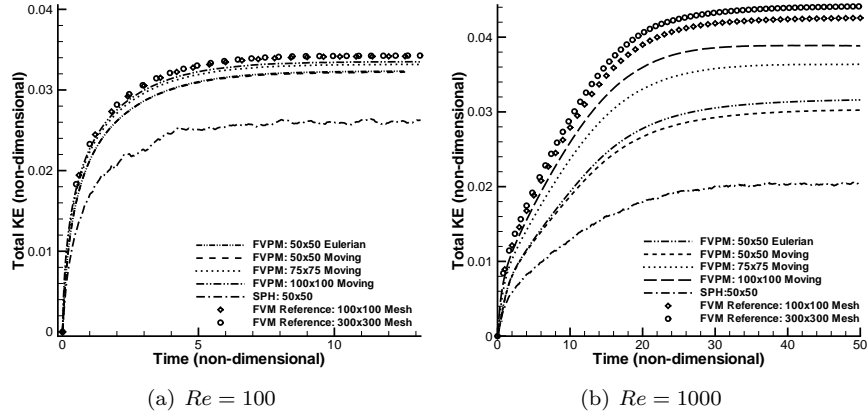

Figure 3: Total kinetic energy histories for lid-driven cavity flow.

The steady state x-component of velocity along the vertical cavity centreline is compared with the computational results of Ghia *et al.* [35] and reference finite volume solutions generated with the OpenFOAM open-source package [36] with uniform 300×300 and 100×100 meshes, and a PISO algorithm. Weakly compressible SPH results by Basa *et al.* [37] using the viscosity model of Cleary [38] and 50×50 particles are included for additional comparison with the FVPM solution.

Figure 1 shows a comparison of FVPM and reference x-velocity profiles along the vertical centreline of the cavity. For $Re = 100$, the FVPM results show good agreement with the finite volume reference solution and that of Ghia *et al.* [35]. In addition, the FVPM results show better agreement with the reference solutions than SPH at equivalent particle numbers. At $Re = 1000$, FVPM is evidently slightly less accurate than the finite volume solution on a 100×100 mesh, which in turn is not converged on the solution of the 300×300 mesh and Ghia *et al.* This discrepancy between FVPM and FVM is due at least in part to the overlap of FVPM particles, which results in a larger effective stencil than in the finite volume method.

The steady-state velocity field for 50×50 particles is plotted in Figure 2. For $Re = 1000$ and 100×100 particles (not shown), the FVPM predicts the x and y extents of the lower right corner vortex as 0.3540 and 0.3200 respectively, which agree within 0.1% and 5.5% with the results of Ghia *et al.* [35]. In Figure 3 we compare the total kinetic energy history of the particles for FVPM, SPH and FVM solutions. FVPM results for 50×50 Eulerian particles are also included to assess the influence of particle motion on the solution. Again, FVPM shows closer agreement with the FVM reference than SPH at equivalent resolution, and as the particle number is increased, the FVPM values converge towards the FVM reference. There is only a small difference in kinetic energy between the results for fixed and moving particles.

3.2. Circular cylinder in crossflow at Reynolds numbers of 20, 40 and 100

Crossflow over a fixed, rigid circular cylinder is one of the classic problems of fluid mechanics and has been the subject of much experimental and numerical investigation. The moving boundary FVPM implementation may be validated by considering the problem in the alternative reference frame in which the cylinder translates through an initially stagnant fluid. This approach has been adopted in previous validations of moving boundary CFD algorithms by Russell and Wang [39] and Le *et al.* [40].

The flow at Reynolds numbers (based on cylinder diameter d and inlet velocity u_∞) 20 and 40 is characterised by the development of a pair of steady recirculation regions in the wake of the cylinder. Above $Re_d \approx 45$ the flow field becomes unsteady, and vortices are periodically shed in the wake of the cylinder [41, 42]. The drag and lift forces in this regime are characterised by periodic oscillations about a mean value and zero respectively. Numerical and experimental data are available in the literature for the non-dimensional drag and lift coefficients C_D and C_L. For steady flow, the length of the recirculation

region L_w in the cylinder wake may also be used for comparison. Validation of the FVPM results is performed on the basis of these parameters.

The total drag and lift coefficients comprising pressure and viscous components of drag and lift, are defined as

$$C_D \quad = \quad \frac{F_x}{\frac{1}{2}\rho u_\infty^2 d} \tag{50}$$

$$C_L \quad = \quad \frac{F_y}{\frac{1}{2}\rho u_\infty^2 d}, \tag{51}$$

where u_∞ denotes the inlet or cylinder velocity for the fixed and translating cases respectively. F_x and F_y are the x and y components of total force on the cylinder surface

$$F_x = \int_{\partial\Omega} f_x n_x \, d\eta, \tag{52}$$

where f_x is the x-component of the pressure and viscous force on the cylinder surface, and n_x is the x-component of the outward (away from domain) normal at the cylinder surface. F_x is approximated in FVPM by

$$F_x \approx \sum_i \left|\boldsymbol{\beta}_i^b\right| \left(p_i^b n_x - n_y \tau_i^b \right), \tag{53}$$

for all particles i interacting with the cylinder. The boundary pressure is extrapolated to the boundary i.e. $p_i^b = p_i$, and the boundary viscous stress τ_i^b is computed using the SPH gradient approximation Eq. (22). A similar approximation is employed for F_y. The coefficient of pressure is defined as

$$C_p(\theta) = \frac{p(\theta) - p_\infty}{\frac{1}{2}\rho u_\infty^2}, \tag{54}$$

where $\theta = 0$ at the stagnation point on the cylinder surface and p_∞ is the freestream pressure. In the periodic vortex shedding regime, the dimensionless vortex-shedding frequency or Strouhal number may be compared with published values. The Strouhal number is defined as

$$St = \frac{fd}{u_\infty}, \tag{55}$$

where f is the vortex shedding frequency. f is taken as the frequency of the C_L oscillations.

Throughout the majority of the domain, the particles are initialised in a uniform Cartesian distribution with spacing $\Delta x_0 \simeq (0.13)d$. The particle distribution is refined within a distance of $(0.8)d$ from the cylinder centre, with a spacing of $\Delta x_0/2$ on the surface. The smoothing length is set to 0.7 times the local particle spacing (or equivalently, the particle support diameter is 2.8 times the particle spacing). In these tests, the boundary interaction vectors are computed via the summation condition, Eq. (45).

Table 1: Flow over a fixed circular cylinder at $Re_d = 20$ and $Re_d = 40$: comparison of recirculation length and drag coefficient with values from literature.

	$Re_d = 20$		$Re_d = 40$	
	L_w/d	C_D	L_w/d	C_D
FVPM	0.86	2.10	2.21	1.57
Experimental:				
Tritton [43]	–	2.22	–	1.48
Coutanceau and Bourard [41]	0.73	–	1.89	–
Computational:				
Fornberg [44]	0.91	2.00	2.24	1.50
Dennis and Chang [45]	0.94	2.05	2.35	1.52
Calhoun [46]	0.91	2.19	2.18	1.62
Russell and Wang [39]	0.94	2.13	2.29	1.60
Ye *et al.* [47]	0.92	2.03	2.27	1.52
Koumoutsakos and Leonard [48]	–	–	–	1.69
Le *et al.* [40]	0.93	2.05	2.22	1.56

3.2.1. Fixed circular cylinder

For the fixed cylinder, the computational domain is a rectangular region containing a cylinder of diameter d. The cylinder centre is located $15d$ downstream of an inlet boundary condition, and $75d$ upstream of an outlet boundary condition. Free-slip wall boundary conditions are specified on the top and bottom sides of the domain, which are located $(7.5)d$ either side of the cylinder centre. The total number of particles is approximately $75,000$. The x-component of inlet velocity and the initial fluid velocity in the domain are set to u_∞. The particles are Eulerian, i.e. $\dot{\mathbf{x}} = 0$.

The steady state pressure and velocity fields at $t^* = tu_\infty/d = 80$ for $Re_d = 20$ and $Re_d = 40$ are shown in Figures 4(a) and 4(b). Table 1 gives a comparison between the present steady state C_D and L_w values with those from the literature for Reynolds numbers 20 and 40. All of the computational studies report a lower value for the drag coefficient than the corresponding experimental results. The FVPM drag coefficients and recirculation lengths agree quite closely with previous computational results at both Reynolds numbers.

The flow has been simulated in the vortex shedding regime at Reynolds number 100. Instantaneous pressure and velocity fields for this flow at $t^* = 150$ are shown in Figure 4(c), illustrating the asymmetric nature of the wake. In Table 2 the mean drag coefficient and amplitude of drag and lift coefficient oscillations in the vortex shedding regime are compared with previously published values. FVPM slightly underpredicts drag and lift coefficients, and good agreement is achieved with previously published data for the Strouhal number.
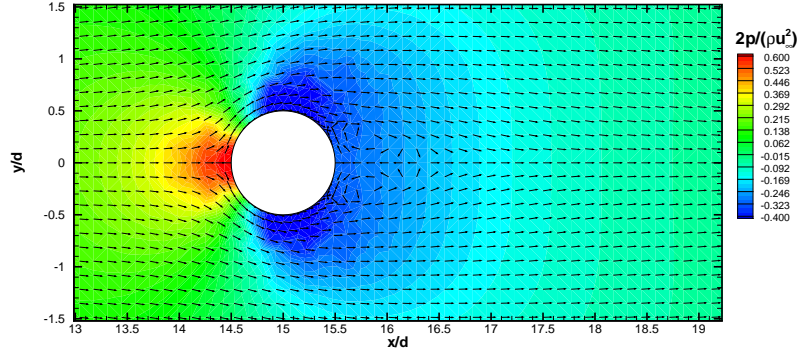
(a) $Re_d = 20, t^* = 80$
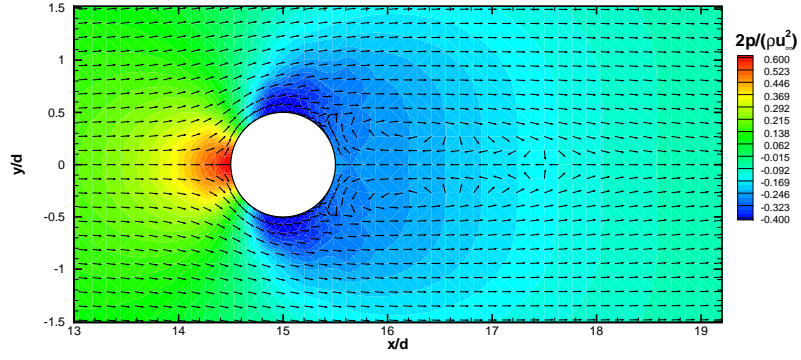
(b) $Re_d = 40, t^* = 80$
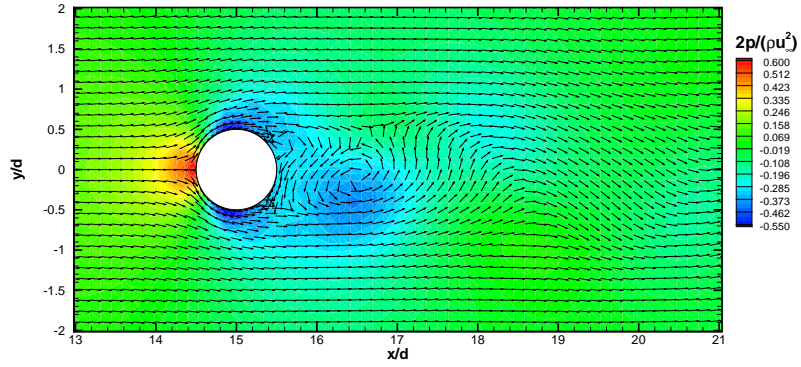
(c) $Re_d = 100, t^* = 150$

Figure 4: Pressure contours and velocity vectors for fixed circular cylinder in crossflow. For clarity, the velocity vectors are shown with uniform length.

18

Table 2: Flow over a fixed circular cylinder at $Re_d = 100$: comparison of mean drag and lift coefficients in the vortex shedding regime with values from literature. Amplitudes are given for the fluctuating components of C_D and C_L.

	C_D	C_L	St
FVPM	1.24 ± 0.010	± 0.225	0.160
Experimental:			
Williamson [49]	–	–	0.160
Computational:			
Braza *et al.* [50]	1.36 ± 0.015	± 0.250	–
Calhoun [46]	1.33 ± 0.014	± 0.298	0.175
Liu *et al.* [51]	1.35 ± 0.012	± 0.339	0.164
Russell *et al.* [39]	1.38 ± 0.007	± 0.300	0.169
Le *et al.* [40]	1.37 ± 0.009	± 0.323	0.160

3.2.2. Translating circular cylinder

The circular cylinder problem may be re-considered in the alternate reference frame in which the fluid is initially at rest, and the cylinder translates through the domain. This amounts to a challenging problem, involving large displacements of the moving boundary and complex flow phenomena. The C_D, C_L and St values may be directly compared with results in section 3.2.1 for flow over a stationary cylinder.

For $Re_d = 20$ and $Re_d = 40$, the domain is $90d$ in the streamwise direction, with $75,000$ particles. The cylinder is initially located at $x/d = 80$. For $Re_d = 100$ a larger domain is necessary due to the longer physical time (and hence larger cylinder displacement) required for the establishment of periodic vortex shedding behaviour. For $Re_d = 100$, the streamwise dimension is $190d$, with $142,000$ particles, and the cylinder is initially located at $x/d = 180$, $y/d = 0$. For all Reynolds numbers, the transverse width of the domain is $15d$. The fluid velocity is initially zero everywhere, and the imposed velocity at the left boundary is zero. Free-slip wall conditions are imposed on the boundaries at $y/d = \pm(7.5)d$. An outlet boundary condition, described in section 2.7, is imposed on the remaining outer boundary. The cylinder accelerates from rest to a constant velocity u_∞, as shown in Figure 5.

It is desirable to maintain the refined particle distribution near the cylinder surface, where high gradients occur. Therefore, the particles within $(0.8)d$ of the cylinder centre move with a prescribed velocity equal to that of the cylinder. Particles in the region $x_c(t) - 5d < x < x_c(t) + 10d$, where $x_c(t)$ is the x-coordinate of the cylinder centre, are allowed to move with nearly Lagrangian corrected motion, with $C = 1/100$ in Eq. (26). Since geometric coefficients are re-computed at each timestep for particles in this region only, this results in a significant saving of computational effort. The remaining particles in the domain are fixed. This problem illustrates the flexibility of a mesh-free technique to enable an arbitrary Lagrangian-Eulerian scheme to suit the needs of the problem
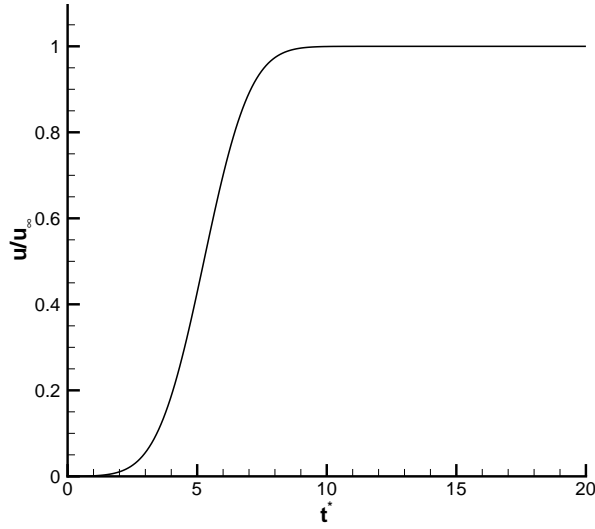
Figure 5: Translating cylinder velocity history.

Table 3: Comparison of C_D, C_L and St values for fixed and moving circular cylinders.

	$Re_d = 20$		$Re_d = 40$		$Re_d = 100$		
	C_D	L_w/d	C_D	L_w/d	C_D	C_L	St
Fixed	2.10	0.86	1.57	2.21	1.24 ± 0.01	±0.225	0.160
Moving	2.08	0.85	1.55	1.89	1.21 ± 0.01	±0.240	0.169

at hand, without restrictions due to the possibility of mesh degradation. This use of the ALE capability of FVPM is quite distinct from the near-Lagragian corrected particle motion described in section 2.5.

As for the fixed cylinder, a steady state solution is expected for $Re_d = 20$ and $Re_d = 40$, with vortex-shedding behaviour at $Re_d = 100$. The pressure and velocity fields (relative to the cylinder) are shown in Figure 6. For $Re_d = 20, 40$ the steady nature of the flow allows direct comparison with Figure 4 for the fixed cylinder case at equivalent resolution. For the moving cylinder, the FVPM accurately predicts the length of the recirculation region and the pressure field at both Reynolds numbers. At $Re_d = 100$ a meaningful comparison of the field values at the same t^* is not possible due to the differing start-up regimes. The drag coefficients for all Re_d agree closely with the fixed cylinder case at equivalent particle resolution, as shown in Table 3. In addition, for $Re_d = 100$ the amplitude of lift coefficient oscillations and the Strouhal number compare well with the fixed cylinder case.
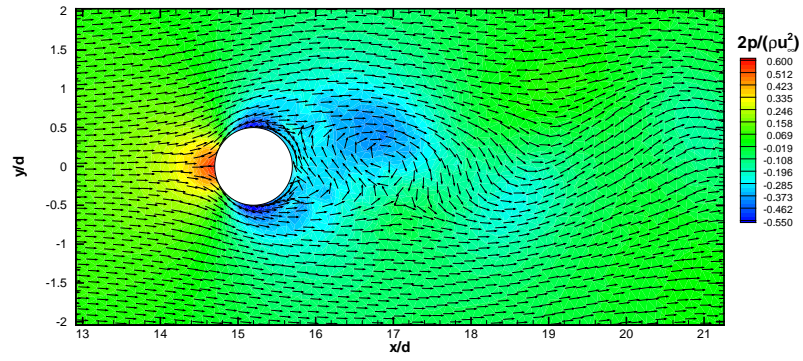
The surface pressure distribution $C_p(\theta)$ is shown in Figure 7 for fixed and

20
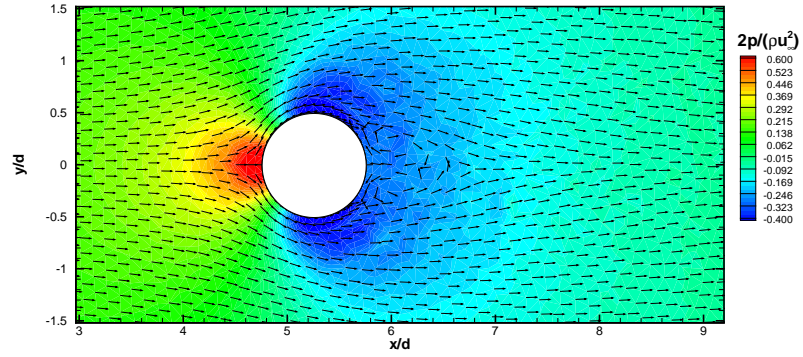
(a) $Re_d = 20, t^* = 80$
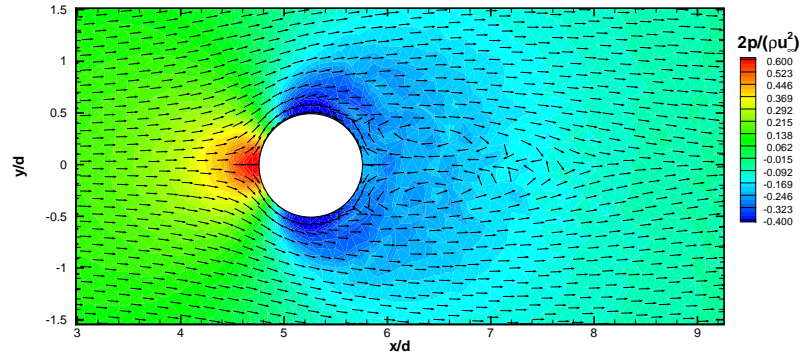
(b) $Re_d = 40, t^* = 80$

(c) $Re_d = 100, t^* = 150$

Figure 6: Pressure contours and velocity vectors (relative to the cylinder) for moving circular cylinder flow. For clarity, the velocity vectors have uniform length.
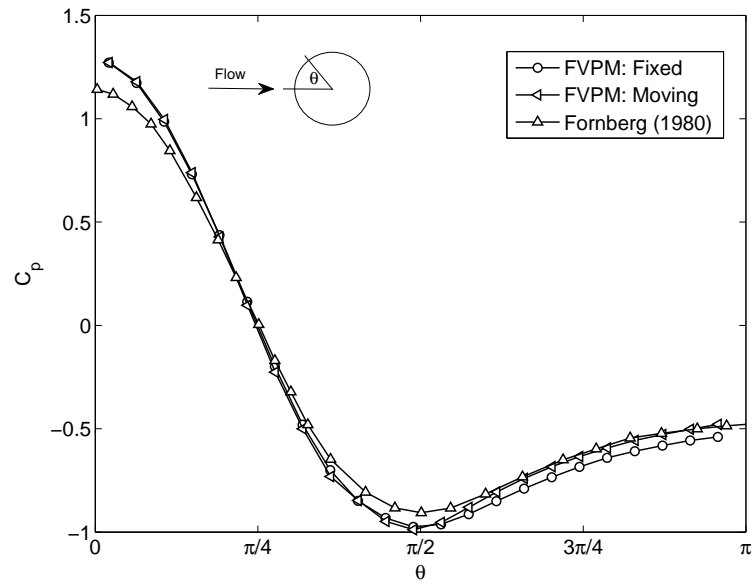
21

Figure 7: Pressure coefficient as a function of position on the cylinder surface for $Re_d = 40$. FVPM results are shown for both the fixed and translating cylinder cases. For the fixed case, the refined discretisation is also included. The result of Fornberg [44] is included for comparison.

moving cylinders at $Re_d = 40$, along with the result of Fornberg [44] for comparison. The FVPM results for the fixed and translating cylinders agree closely with each other and the reference solution, affirming the accuracy of the present FVPM formulation for viscous incompressible flow with boundary motion.

4. Conclusions

A fully incompressible implementation of the FVPM for viscous flows with moving walls has been presented and validated. Following previous FVPM work, the fully incompressible formulation is based on a standard pressure projection technique with an explicit temporal discretisation. Viscous modeling is implemented on the basis of consistency-corrected SPH gradient approximations, and the particles are moved with arbitrary Lagrangian-Eulerian (but nearly Lagrangian) motion to prevent the formation of poor particle distributions. A novel formulation was introduced for computation of particle volume rate of change, and has been proven to ensure the preservation of uniform fields for any particle motion field. The method has been validated for lid-driven cavity flow at Reynolds numbers up to 1000, for which FVPM demonstrates good agreement with reference data. For flow over a fixed circular cylinder at Reynolds numbers up to 100, the FVPM computations for drag, lift, surface pressure distribution and vortex shedding frequency show good agreement with computational and experimental reference values from literature. Non-uniform particle distributions were used in the cylinder flow problem to enhance local resolution near the cylinder. The method was validated for large-displacement moving boundary problems by considering the cylinder flow in an alternative reference frame in which the cylinder translates through a stagnant fluid at Reynolds numbers up to 100. The force coefficients and vortex shedding frequencies for the moving cylinder show good agreement with those for the fixed cylinder.

The FVPM is attractive as a mesh-free method for fluid dynamics because local conservation is ensured and boundary conditions may be enforced without the need for fictitious particles. Its similarity with the finite volume method means that many established CFD techniques can be directly implemented in the FVPM. The test cases presented in this article demonstrate that the FVPM, in an arbitrary Lagrangian-Eulerian framework with corrected Lagrangian particle motion, is a powerful and flexible tool for simulation of large-displacement moving boundary flows.

23

References

[1] R. Gingold, J. Monaghan, Smoothed particle hydrodynamics: theory and application to non-spherical stars, Monthly Notices of the Royal Astronomical Society 181 (1977) 375–389.

[2] L. Lucy, A numerical approach to testing the fission hypothesis, The Astronomical Journal 82 (1977) 1013–1924.

[3] J. J. Monaghan, Smoothed particle hydrodynamics, Reports on Progress in Physics 68 (2005) 1703–1759.

[4] M. Gómez-Gesteira and Robert A. Dalrymple, Using a Three-Dimensional Smoothed Particle Hydrodynamics Method for Wave Impact on a Tall Structure, Journal of Waterway, Port, Coastal, and Ocean Engineering 130 (2004) 63–69.

[5] T. Belytschko, Y. Krongauz, D. Organ, M. Fleming, P. Krysl, Meshless methods: An overview and recent developments, Computer Methods in Applied Mechanics and Engineering 139 (1996) 3–47.

[6] N. Quinlan, M. Lastiwka, M. Basa, Truncation error in mesh-free particle methods, International Journal for Numerical Methods in Engineering 66 (2006) 2064–2085.

[7] P. Randles, L. Libersky, Smoothed particle hydrodynamics: some recent improvements and applications, Computer Methods in Applied Mechanics and Engineering 139 (1996) 375–408.

[8] J. Bonet, T.-S. L. Lok, Variational and momentum preservation aspects of smooth particle hydrodynamic formulations, Computer Methods in Applied Mechanics and Engineering 180 (1999) 97–115.

[9] T. Ismagilov, Smooth volume integral conservation law and method for problems in Lagrangian coordinates, Computational Mathematics and Mathematical Physics 46 (2006) 453–464.

[10] J. P. Vila, On particle weighted methods and smoothed particle hydrodynamics, Mathematical models and Methods in Applied Sciences 9 (1999) 161–209.

[11] J. Monaghan, SPH and Riemann Solvers, Journal of Compuational Physics 136 (1997) 298–307.

[12] D. Hietel, K. Steiner, J. Struckmeier, A finite volume particle method for compressible flows, Mathematical Models and Methods in Applied Science 10 (2000) 1363–1382.

[13] C. Schick, Adaptivity for particle methods in fluid dynamics, Master's thesis, University of Kaiserslautern (2000).

[14] D. Teleaga, J. Struckmeier, A finite-volume particle method for conservation laws on moving domains, International Journal for Numerical Methods in Fluids 58 (2008) 945–967.

[15] D. Teleaga, A finite volume particle method for conservation laws, Ph.D. thesis, University of Kaiserslautern (2005).

[16] R. Keck, The finite volume particle method: A meshless projection method for incompressible flow, Ph.D. thesis, University of Kaiserslautern (2002).

[17] R. Keck, D. Hietel, A projection technique for incompressible flow in the meshless finite volume particle method, Advances in Computational Mathematics 23 (2005) 143–169.

[18] R. Nestor, M. Basa, M. Lastiwka, N. Quinlan, Extension of the finite volume particle method to viscous flow, Journal of Computational Physics 228 (2009) 1733–1749.

[19] M. Junk, Do finite volume methods need a mesh?, Lecture Notes in Computational Science and Engineering, Springer, 2003, pp. 223–238.

[20] D. Hietel, R. Keck, Consistency by coefficient correction in the finite volume particle method, in: M. Griebel (Ed.), Meshfree Methods for Partial Differential Equations, Lecture Notes in Computational Science and Engineering, Springer, Berlin, 2003, pp. 211–221.

[21] B. van Leer, Towards the ultimate conservative difference scheme. V - a second-order sequel to Godunov's method, Journal of Computational Physics 32 (1979) 101–136.

[22] J. Monaghan, J. Lattanzio, A refined method for astrophysical problems, Astronomy and Astrophysics 149 (1985) 135–143.

[23] T. Barth, D. Jespersen, The design and application of upwind schemes on unstructured meshes, in: AIAA 27th Aerospace Sciences Meeting, AIAA, Reno, 1989.

[24] D. Drikakis, W. Rider, High-resolution methods for incompressible and low-speed flows, Springer, Berlin, 2005.

[25] A. Harten, P. Lax, B. Van Leer, On upstream differencing and Godunov-type schemes for hyperbolic conservation laws, SIAM Review 25 (1983) 35–61.

[26] R. Klein, Semi-implicit extension of a Godunov-type scheme based on low Mach number asymptotics I: one-dimensional flow, Journal Computational Physics 121 (1995) 213–237.

[27] T. Schneider, N. Botta, K. Geratz, R. Klein, Extension of finite volume compressible flow solvers to multi-dimensional, variable density zero mach number flows, Journal of Computational Physics 158 (2000) 248–286.

25

[28] C. Hirsch, Numerical computation of internal and external flows, volume 2: computational methods for inviscid and viscous flows, Wiley, Chichester, 1988.

[29] A. Chorin, Numerical solution of the Navier-Stokes equations, Mathematics of Computation 22 (1968) 745–762.

[30] J. Ferziger, M. Peric, Computational Methods for Fluid Dynamics, Springer, Berlin, 2002.

[31] T. Skalicky, Laspack 1.12.2 (1995).
URL http://dddas.org/mgnet/Codes/laspack/html/laspack.html

[32] J. Morris, P. Fox, Y. Zhu, Modelling low Reynolds number incompressible flows using SPH, Journal of Computational Physics 136 (1997) 214–226.

[33] D. Anderson, Computational fluid dynamics: the basics with applications, McGraw-Hill, London, 1995.

[34] S. Watkins, A. Bhattal, N. Francis, J. Turner, A. Whitworth, A new prescription for viscosity in smoothed particle hydrodynamics, Astronomy and Astrophysics Supplement Series 119 (1996) 177–187.

[35] U. Ghia, K. Ghia, C. Shin, High-Re solutions for incompressible flow using the Navier-Stokes equations and a multigrid method, Journal of Computational Physics 48 (1982) 387–411.

[36] OpenCFD Ltd., OpenFOAM 1.4.1, www.opencfd.co.uk, (Accessed: 8 Aug. 2008).

[37] M. Basa, N. Quinlan, M. Lastiwka, Robustness and accuracy of SPH formulations for viscous flow, International Journal for Numerical Methods in Fluids.

[38] P. Cleary, Modelling confined multi-material heat and mass flows using SPH, Applied Mathematical Modelling 22 (1998) 981–993.

[39] D. Russell, Z. J. Wang, A cartesian grid method for modeling multiple moving objects in 2d incompressible viscous flow, Journal of Computational Physics 191 (2003) 177–205.

[40] D. Le, B. Khoo, J. Peraire, An immersed interface method for viscous incompressible flows involving rigid and flexible boundaries, Journal of Computational Physics 220 (2006) 109–138.

[41] M. Coutanceau, R. Bouard, Experimental determination of the main features of the viscous flow in the wake of a circular cylinder in uniform translation. part 1. steady flow, Journal of Fluid Mechanics 79 (1977) 231–256.

[42] D. P. Jackson, A finite-element study of the onset of vortex shedding in flow past variously shaped bodies., Journal of Fluid Mechanics 182 (1987) 23–45.

[43] D. Tritton, Experiments on the flow past a circular cylinder at low reynolds numbers, Journal of Fluid Mechanics 6 (1959) 547–567.

[44] B. Fornberg, A numerical study of steady viscous flow past a circular cylinder, Journal of Fluid Mechanics 98 (1980) 819–855.

[45] S. C. R. Dennis, G.-Z. Chang, Numerical solutions for steady flow past a circular cylinder at Reynolds numbers up to 100, Journal of Fluid Mechanics 42 (1970) 471–489.

[46] D. Calhoun, A cartesian grid method for solving the two-dimensional streamfunction-vorticity equations in irregular regions, Journal of Computational Physics 176.

[47] T. Ye, R. Mittal, H. Udaykumar, W. Shyy, An accurate cartesian grid method for viscous incompressible flows with complex immersed boundaries, Journal of Computational Physics 156 (1999) 209–240.

[48] P. Koumoutsakos, A. Leonard, High-resolution simulations of the flow around an impulsively started cylinder using vortex methods, Journal of Fluid Mechanics 296 (1995) 1–38.

[49] C. Williamson, Oblique and parallel modes of vortex shedding in the wake of a circular cylinder at low reynolds numbers, Journal of Fluid Mechanics 206 (1989) 579–627.

[50] M. Braza, P. Chassaing, H. Ha Minh, Numerical study and physical analysis of the pressure and velocity fields in the near wake of a circular cylinder, Journal of Fluid Mechanics 165 (1986) 79–130.

[51] C. Liu, X. Zheng, C. H. Sung, Preconditioned multigrid methods for unsteady incompressible flows, Journal of Computational Physics 139 (1998) 35–57.